APPLIED SCIENCES AND ENGINEERING

Continuous operation of battery-free implants enables advanced fracture recovery monitoring

Kevin Albert Kasper[1], Gerardo Figueroa Romero[1,2], Dania L. Perez[1], Avery M. Miller[1], David A. Gonzales[2], Jesus Siqueiros[1], David S. Margolis[1,2,3]*, Philipp Gutruf[1,4]*

Substantial hurdles in achieving a digitally connected body with seamless, chronic, high-fidelity organ interfaces include challenges of sourcing energy and ensuring reliable connectivity. Operation is currently limited by batteries that occupy large volumes. Wireless, battery-free operation is therefore paramount, requiring a system-level solution that enables seamless connection of wearable and implantable devices. Here, we present a technological framework that enables wireless, battery-free implant operation in freely moving subjects, with streaming of high-fidelity information from low-displacement, battery-free implants with little user interaction. This is accomplished using at-distance wirelessly recharged, wearable biosymbiotic devices for powering and communication with fully implantable NFC-enabled implants. We demonstrate this capability with osseosurface electronics that stream bone health insight. Eleven-month-long large animal studies highlight the ability of implants to relay information on bone health without negative impact on the subjects. Clinical translatability is shown through fracture healing studies that demonstrate biomarkers of bone union.

INTRODUCTION

Continuous collection of biosignals offers profound benefits in refining diagnostic accuracy (*1*–*3*), personalizing patient care (*4*–*6*), and assessing disease progression and intervention efficacy (*7*–*9*). Implantable devices, which can sample with higher sensitivity and improved measurement accuracy relative to wearable medical devices, further enhance the benefits of continuous biosignal collection (*10*, *11*).

Traditionally, continuous operation of implantable devices relies upon electrochemical power storage, such as batteries, which suffers from several limitations: finite lifetimes, limited energy storage capacity, and size restrictions due to space limitations at the target site. Wireless charging techniques enable implantable devices with smaller, rechargeable batteries that increase functional lifetimes, extend potential biological targets, and permit more demanding applications (*12*, *13*). Still, rechargeable batteries have a finite number of cycles, with overall efficiency decreasing over time, and battery size continues to impose limitations on target sites and device architectures (*14*).

Recent work in implantable medical devices highlights the advantages of electronics powered entirely through wireless power transfer (WPT) technologies, such as through ultrasound, light, or near-field coupling (*12*, *15*–*17*). These wireless systems avoid performance degradation from battery power supplies and inherently increase functional lifetimes relative to battery powered implants, which must be recharged or replaced. In addition, they offer markedly reduced displacement volumes and the opportunity to create devices with soft mechanics (*18*) that decrease tissue irritation (*19*) and facilitate insertion using less-invasive implant methods (*20*). Despite numerous advantages, applications of this device class remain limited by current system-level WPT approaches (*16*).

Continuous power delivery to implantable wireless, battery-free (WBF) systems in large animal models and humans is a critical technological bottleneck impeding widespread adoption and clinical relevance. The few existing clinical WBF implants use tethered power casting or large, bulky battery packs, which are inconvenient at best and prohibitive or exclusionary in some applications (*21*, *22*). Compact battery-powered wearables for powering WBF implants exist; however, they are primarily used for short-term interfacing (*23*–*26*). While battery-powered wearables for WPT allow the freedom of movement, they must be frequently removed to be recharged, which leads to intermittent data and function loss (*27*) and can contribute to patient noncompliance over time (*28*).

There are currently no practical solutions for long-term deployment of WBF implants, especially when considering populations that may not be capable of managing their own care. There is a need for system-level design which can realistically be adopted by users of all abilities. To facilitate seamless utilization of WBF implantable devices over chronic timescales in freely moving patients without needing to manage battery life, we introduce a wireless, wearable, biosymbiotic hub (BH) for battery-free implants, illustrated in Fig. 1A. This wearable device transfers power and exchanges data with WBF implantable electronics over chronic timescales, enabling sustained operation of chronic biointerfaces, exemplified by osseosurface electronics (the implantable biointerface shown in Fig. 1A, inset) (*29*). Leveraging far-field power transfer capabilities of biosymbiotic electronics (*30*), the system design enables wireless recharging at a distance, obviating the need for device removal and manual recharging. Autonomous operation, achieved using ultralow-power bluetooth low energy (BLE) (*30*) and near-field communication (NFC) controllers, and on-body recharging mean that no interaction is required from the wearer at any point, extending data acquisition over weeks to months, only limited by mechanical and electrical integrity of the wearable (*27*).

This continuously operating implant interface enables patient monitoring and recovery tracking and, when paired with an existing

[1]Department of Biomedical Engineering, University of Arizona, Tucson, AZ 85721, USA. [2]Department of Orthopaedic Surgery, University of Arizona, Tucson, AZ 85721, USA. [3]Department of Physiological Sciences, Bio5 Institute, University of Arizona, Tucson, AZ 85721, USA. [4]Departments of Electrical and Computer Engineering, Bio5 Institute, Neuroscience GIDP, University of Arizona, Tucson, AZ 85721, USA.
*Corresponding author. Email: dsm@arizona.edu (D.S.M.); pgutruf@arizona.edu (P.G.)

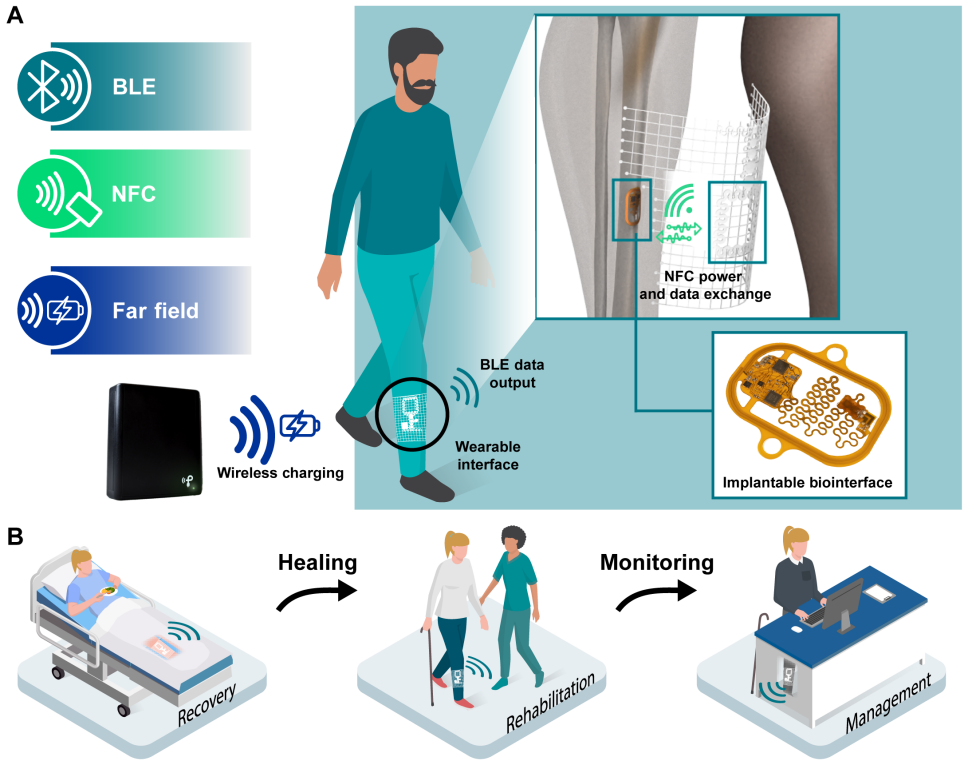

Fig. 1. Continuously operating wearable device for powering and communicating with WBF NFC-capable implantable electronics. (**A**) System overview demonstrating implementation of wireless far-field charging of the wearable device, BLE data output from wearable, and NFC power and data transfer with an implantable biointerface, e.g., an osseosurface strain sensor (*29*). (**B**) Illustration showing applications of wearable device in patient recovery monitoring, post-surgical rehabilitation, and long-term disease management.

WBF implant, serves as a sensing and stimulation control interface during long-term disease management (shown in Fig. 1B).

Impact of this technological framework is demonstrated using osseosurface electronics (*29*), which exhibit characteristics such as growth to the bone and materials that are safe to use over subject lifetimes. These characteristics enable placement during routine surgery to characterize bone health over many months, without the need for device recovery after the diagnostic and therapeutic window. Osseosurface electronics, when paired with the BH, enable substantial monitoring capability that can assess bone health and healing with a precision currently unmatched, paving the way for targeted, effective therapeutic interventions and consistency in fracture healing assessment.

RESULTS

Indefinite operation of wearable and implant

Biosymbiotic architecture describes a class of devices that enable autonomous, multimodal data recording without interaction from the wearer in a form factor that is tailored to the individual, lightweight, and adhesive-free, promoting extended wear with nearly imperceptible operation (*30*–*33*). The BH, photo shown Fig. 2A (top), takes advantage of modern NFC technology to power and exchange data with WBF NFC-capable devices implanted up to several centimeters deep in the body. Figure 2A (middle) details the core functionality enabled by each of the three onboard antennas. Electronics are physically separated onto functional islands joined via serpentine-patterned interconnects. This design approach, combined with a self-similar serpentine-patterned rectangular coil NFC antenna, enables system-level stretchability and strain tolerance critical for everyday wear (*30*, *34*). Encapsulation using flexible ultraviolet (UV)-cure resin provides resistance to mechanical and liquid damage while maintaining flexibility.

Figure 2B details operating principles of the wearable device that enable power transfer and communication with implantables over chronic timescales without manual battery management. Far-field power transferred from commercially available 915-MHz power casting systems is harvested by the BH using a serpentine-structured dipole antenna, which is extensively characterized in (*30*). Harvested power is regulated using a low-dropout voltage regulator (LDO) and used to charge a lithium polymer (LiPo) battery which feeds the ultralow-power electronics continuously and buffers high drain events during implant powering and readout. Federal Communications Commission (FCC)-approved, commercially available far-field power casting systems provide rechargeability up to 2 m and can be placed in areas where subjects spend most of their time, as determined by behavioral analysis (*31*). Prior work in biosymbiotic technology characterizes the charging ability and limitations of far-field power transfer for this device class (*30*–*33*). The BLE microcontroller on the BH handles communication with external systems, processes data received over NFC, and controls the NFC initiator-reader integrated circuit (IC) that generates the 13.56-MHz near field for power transfer and communication with NFC-enabled implants. Detailed system schematic is shown in fig. S1. Antenna

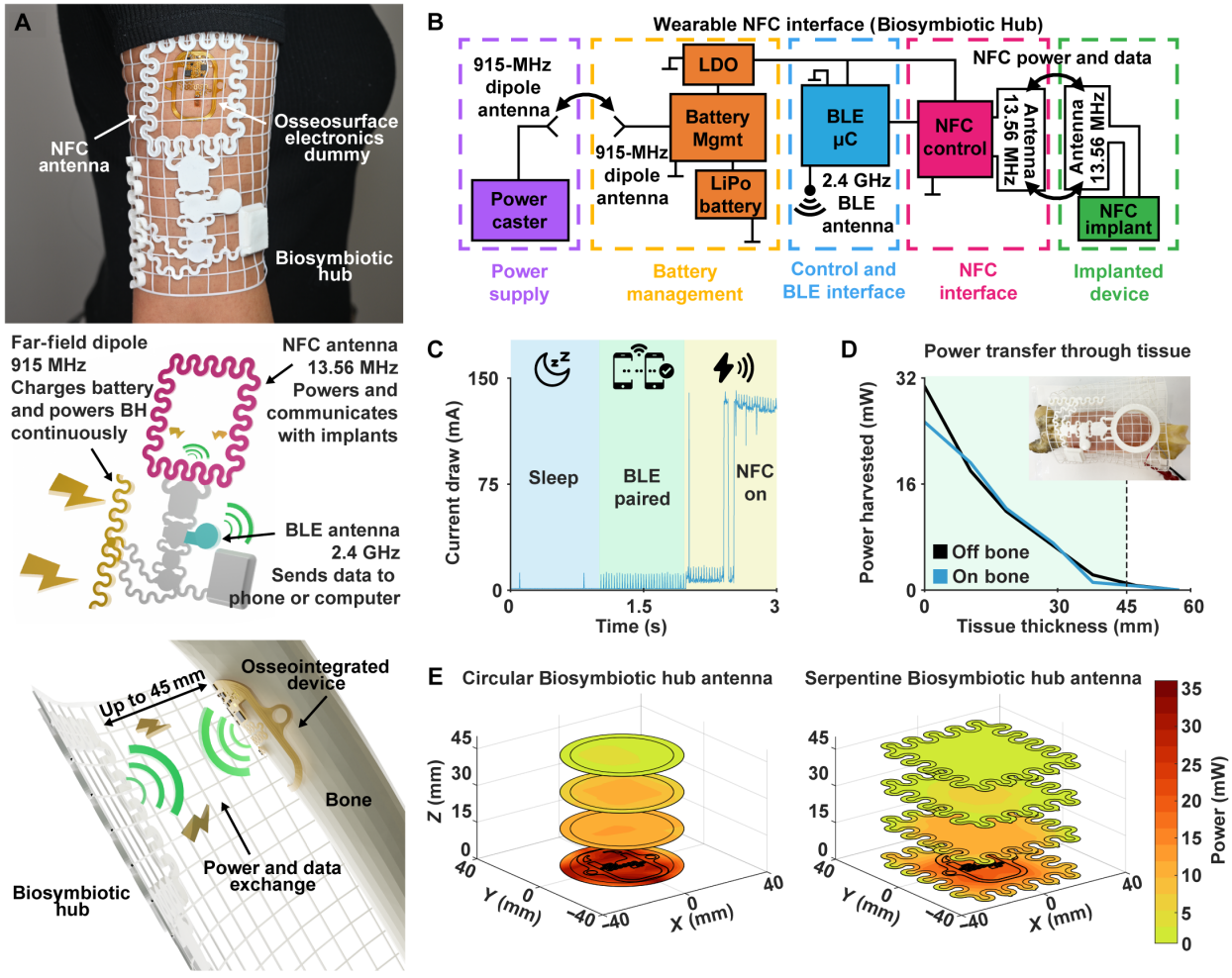

Fig. 2. Continuously operating, wearable battery-free implant interface design. (**A**) Photograph of BH on arm (top). Osseosurface electronics dummy epidermally adhered in center of serpentine-structured NFC antenna to simulate operation in humans. A 3D rendering (middle) identifies the three antennas that enable data collection from WBF implants over extended durations. The bottom rendering illustrates data and power exchange between wearable device and implant. (**B**) Functional block diagram for the BH broadly applicable to any NFC-capable device. (**C**) Current consumption of wearable when idling with BLE enabled, connected over BLE to a data logging device, and connected with WPT enabled. (**D**) Power transfer between the BH and osseosurface electronics through porcine tissue of increasing thickness. The typical operating power range of osseosurface electronics is highlighted in green. (**E**) 3D plot of field densities created in open air by the BH with two NFC antenna configurations. Left: Circular, wire-wound four-turn antenna. Right: Serpentine-structured two-turn flexPCB antenna. Size of harvesting antenna is shown at $z = 0$ mm on both plots. LiPo, lithium polymer.

matching and tuning circuitry at the NFC interface allows for straightforward replacement of the NFC antenna to suit different applications, such as larger coverage area or concentrated power delivery for deep tissue implants. In addition, the NFC initiator-reader IC has automatic antenna tuning functionality, allowing real-time corrections to account for detuning as the dielectric environment around the BH changes, such as different clothing (see fig. S2).

While the BH does not need to be charged similar to traditional wearable devices, efficient power management is still necessary to ensure smooth operation between charging events. Figure 2C plots current and power consumption during typical operating scenarios. By default, the BH remains in a low-power sleep with BLE active and the NFC transceiver powered down, consuming <0.5 mW. Upon BLE pairing, the device wakes and increases BLE packet rates to maintain responsiveness. BLE packet exchange events (duration, <3 ms) consume a maximum of 30 mW. During reading periods where the BH is powering and communicating with an implant, power consumption is reliant upon NFC antenna matching but can vary by application between 500 mW and 1.6 W. For shallow tissue applications, the BH with serpentine-structured NFC antenna draws 150 mA during power transfer events. For deeper tissue implants, a smaller, circular wire-wound NFC antenna can be used to concentrate the field, with the BH drawing 250 to 370 mA depending on target depth. Without far-field power harvesting or WPT events, the BH has a lifetime near 6.5 days using a single 0.3-cm^3 30-mAh LiPo cell. This lifetime can be markedly increased (into weeks and months) by disabling the microcontroller's BLE radio and placing the microcontroller into a deep sleep or standby mode, although some trigger, e.g., an accelerometer on the wearable BH monitoring for gait patterns, will need to be implemented to wake the device and enable BLE communication. For detailed lifetime data during different operational modes, see table S1.

Power harvesting of the implant through increasing layers of porcine tissue, shown in Fig. 2D, indicate a peak power availability of 24 to 32 mW on and off bone, respectively, at 0-mm tissue depth when using a circular coil wire-wound NFC antenna. At 30-mm tissue depth, power availability decreases to 8 mW. Power transfer at 13.56 MHz is well characterized (*35*) and considered safe (*12*), with strict regulations by the FCC of 1.6 W/kg (*36*) and the International Commission on Non-Ionizing Radiation Protection (ICNIRP) of 4 W/kg (*37*) limits for specific absorption rate (SAR) in arms and legs. A SAR simulation of the serpentine-coil NFC antenna on the BH, illustrated fig. S3, reveals a SAR of <0.017 W/kg at maximum power output, well below both the FCC and ICNIRP limits. Prior characterization of the 915-MHz power harvesting dipole antenna reveals a maximum SAR of 0.235 W/kg (*30*), also well below federal and international safety regulations.

Under ideal conditions, the maximum data rate for the NFC standard used in this work [International Standards Organization/International Electrotechnical Commission (ISO/IEC) 15693] is 26.48 kilobits/s (kbps) (*38*). For standard 12- or 16-bit fidelity this equates to 2206 and 1655 samples/s, respectively (*39*). Figure S4 shows data transfer rates through tissue on- and off-bone realized by the BH when paired with osseosurface electronics. Analysis shows data acquisition rate from the implant decreases as tissue thickness increases, likely due to increased bit error rate as field amplitude decreases. The data show that the BH can power and read from devices implanted up to 48-mm deep with around 600-Hz sampling rate and 16-bit fidelity. Communication with devices implanted deeper than 48 mm was unreliable for the high sampling rates required for osseosurface electronics; however, the BH's performance may still be acceptable for operations with less stringent requirements up to 60-mm deep.

Shown in Fig. 2E (left) is the spatial distribution of the generated field for a circular four-turn NFC antenna, which is designed for powering deep tissue osseosurface electronics. The field distribution for the serpentine-structured antenna is shown Fig. 2E (right). The serpentine-structured antenna sacrifices field strength and delivery depth, relative to the circular coil antenna, in exchange for stretchability (see fig. S5), conformality, and higher tolerance for implant-BH misalignment (fig. S6).

To demonstrate the adaptability of these powering and communication antennas, implantable device antennas with different geometries—i.e., number of turns, trace thickness and spacing, and shape—are characterized with results shown in fig. S7, featuring power densities from 440.8 to 3101 mW/cm^3. The power harvested by miniaturized WBF implantable antennas (5.1 mm by 9.4 mm, 0.003-cm^3 displacement volume, and 20 mW peak consumption) is sufficient for optical (*40*, *41*) and electrical stimulation (*42*, *43*).

Chronic wearable experiments

Despite the benefits of health and activity tracking, user retention of devices for diagnostics and therapeutics remains an unsolved issue, with comfort and usability as the most cited reasons. Numerous social, cognitive, and psychological factors influence device use; ultimately benefit to burden ratio determines retention (*27*, *44*).

A focus is to eliminate user interaction with the BH. Through biosymbiotic device architecture, which enables uninterrupted operation (*30*, *31*, *33*), data communication over tens of kilometers (*32*), and high fidelity sensing capabilities (*30*, *32*), we achieve total system weight of 23.5 g with one 30mAh battery and an average device thickness of 0.93 mm. Compared to common wearable devices, this is an average profile 12x thinner (0.93 mm vs 12 mm, smartwatch) and a stiffness 13.4% – 16.5% of a tested commercial smartwatch band (fig. S8), providing enhanced comfort over extended durations. The BH minimizes skin contact over the bulk of the device and omits adhesives, encouraging normal skin turnover and preventing irritation arising from accumulation of sweat, foreign particles, and skin debris. Coupled with far field power casting, this enables continuous wear and uninterrupted data streams. The continuously operating BH can be worn while sleeping and during exercise (Fig. 3, top). Elastomer encapsulation (see fig. S9) enables continuous wear even in showers.

To demonstrate chronic functionality, i.e., continuous operation of the BH without removal using only far-field power transfer, a chronic wearability experiment is performed. An average sampling rate of 2 recording sessions per day is utilized (see table S1) over a two-week period. During each recording session, the NFC reader field is enabled, and mock strain and ambient temperature data are collected at 600 Hz and 10 Hz, respectively, via NFC from an epidermally laminated osseosurface device. Fig. 3 (Bottom) shows battery life over a two-week period. Regions shaded in green indicate charging sessions each day when the wearer was seated at their work desk. Recorded battery voltage remains above 3.7 V during the experiment, well above the required minimum, which is labeled "Battery Empty", demonstrating robust recharging without action by the subject, well aligned with characterization of far field power transfer from prior work characterizing daily availability of power using human behavior experiments (*31*).

Enhanced osseosurface electronics for chronic bone health characterization

Prior work with osseosurface electronics showcases WBF, fully-implantable musculoskeletal biointerfaces capable of high-resolution sensing and stimulation in freely moving small animal subjects in vivo (*29*). When deployed in conjunction with the BH, osseosurface electronics provide detailed insight into bone health over extended durations. To support months of continuous operation in large animal models, integration of digital adjustment of the strain sensing circuitry is necessary to compensate for bias induced during surgery and stages of osseointegration.

Shown in Fig. 4A is a photograph of an osseosurface implant with a serpentine biointerface interconnect that provides strain isolation, promoting osseointegration of the strain gauge by limiting gauge movement during the bone bonding process and enabling attachment in large animal models (*29*). Tabs on either side of the device antenna allow for improved manipulation during surgical implantation and a secure fastening point for resorbable sutures, improving device contact with the osseosurface and minimizing any post-surgical device migration before osseointegration. An exploded layer diagram and circuit diagram in fig. S10 (A and B) indicate circuitry introduced for on-the-fly adjustment of sensing circuit parameters post-implantation, critical for chronic operation in large animal models. Specifically, a digital potentiometer and a variable gain instrumentation amplifier are introduced to enable adjustments of strain sensing parameters to accommodate for induced strain bias as the device bonds to bone. A complete system schematic is included in fig. S11.

Figure S12 shows characterization of high-fidelity strain sensing with a resolution of 0.36 microstrain (με) per analog-to-digital

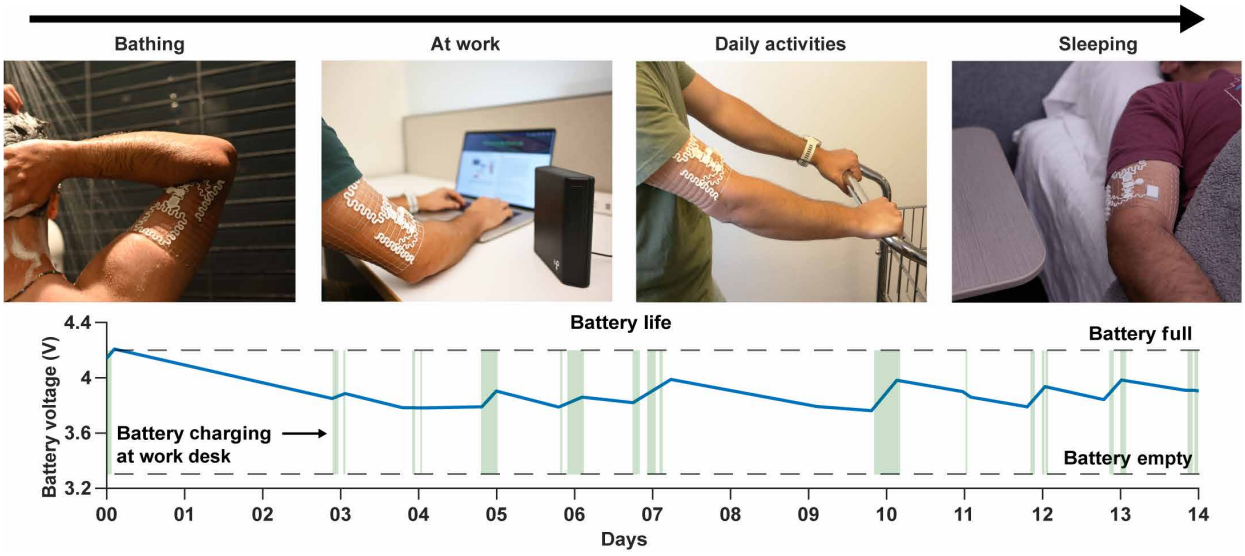

Fig. 3. Chronic wearability experiments. Photograph of typical daily activities supported by the wearable BH. Recharge is enabled when in proximity to power caster located at desk. A 14-day experiment with continuous battery voltage (bottom graph) recordings. The "battery empty" and "battery full" lines indicate the operating limits of the wearable BH. Green sections indicate charging of battery.

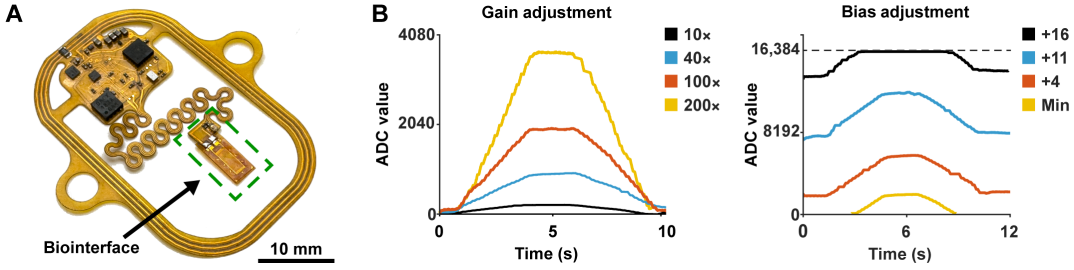

Fig. 4. Osseosurface electronics for chronic bone health characterization. (**A**) Photograph of an osseosurface device. Green dashed outline indicates location of the biointerface, where the strain gauge and thermography sensor are located. (**B**) Demonstration of bone strain acquisition with the ability to digitally adjust gain and biasing of the strain sensing circuit. Bias adjustment units are digital wiper values for 8-bit digital potentiometer. Dashed line in bias adjustment indicates maximum value for 14-bit ADC.

converter (ADC) value, as captured by a 10-bit ADC upsampled to 14-bits, equating to a dynamic range of 5957 με. Bone strain measurement in vivo shows normal ambulatory magnitudes peaking around ~1200 με (*45*), ~2000 to 2200 με (*46*, *47*), and ~2000 με (*48*) for rats, sheep, and humans, respectively, all within engineered dynamic range. The circuits introduced here capture fine detail of strain during loading of a bone sample, shown in fig. S12A, where peak strain of 1181 με at 20-kg loading is visible. Metal foil strain gauges are chosen here due to their high resolution (higher than 0.1 microstrain, με) (*49*) and temperature stability, very fine resistance tolerances (the gauges used in this work guarantee a tolerance of 0.8%), and enhanced cyclic stability compared to other strain sensing techniques, which is critical for continuous operation over extended monitoring periods. While metal foil gauge performance is poor for usage in cartilage and other soft tissues, the deployment of these gauges on cortical bone in vivo limits their exposure to strains beyond their sensing capabilities, with cortical bone having a typical physiological range of ~2000 με (*48*). Continuous thermography allows for early detection of fluctuations in localized tissue temperature to provide a biomarker for acute inflammation or infection. Temperature sensing is included for this reason, although we did not encounter any infection during large animal studies (*50*). Gold-standard comparison with a resolution of 6 mK/ADC value, also captured with a 10-bit ADC upsampled to 14 bits, is shown in fig. S12B.

Shown in Fig. 4B (left) is bone loading data measured by an osseosurface device with gain settings of 10×, 40×, 100×, and 200×. Figure 4B (right) shows the effects of bias adjustment on strain acquisition. These capabilities enable adjustments for any prestrain induced during or after implantation. This combined functionality allows for high sensitivity data collection over months with the ability to adapt to ongoing bone deposition and bone defects, such as fractures and osteoporosis, that result in bone deformation well outside the range of healthy participants.

Large animal studies

Long-term large animal studies are performed to establish baseline clinical readiness of this technological framework with sheep, chosen due to their suitability as an orthopedic model for humans (*51*). Each sheep is implanted with four osseosurface devices. Sensor

placements are illustrated in Fig. 5A (top with insets). The placement of the BH relative to the implants is depicted in Fig. 5A (bottom), with a photograph of the device worn by a sheep shown in Fig. 5B. ISO/IEC standard ISO15693 uses anti-collision mechanisms that allow tolerance of over one hundred overlapping NFC devices, thus multiple osseosurface devices can be highly localized (Fig. 5A, middle inset) and addressed individually (see fig. S13 for simultaneous multidevice data collection measurements), with a maximum data rate of 26.48 kbps split across bidirectional data exchange from all implants. Assuming a sampling rate of 60 Hz (48 Hz is shown to capture at least 90% of the full value of most kinematic impact forces) (*52*), up to 10 osseosurface devices can be theoretically colocated and simultaneously capture clinically relevant data (see table S2 for data rate measurements and calculations).

Shown in Fig. 5C is a lateral view (anteroposterior view shown in fig. S14) x-ray radiograph of a BH aligned over the site of an osseosurface sensor. Routine radiographs locate the implant and relative position needed for the BH with an average misalignment well within the characterization shown in fig. S6.

Osseosurface electronics can measure deep tissue temperature at millikelvin resolution, as shown by measurement of rocking activity yielding elevated temperatures of the quadriceps femoris in Fig. 5D, highlighting the sensing fidelity of this device class. Wireless, high-fidelity bone strain capture in freely moving subjects is demonstrated by rocking of the sheep implanted with the

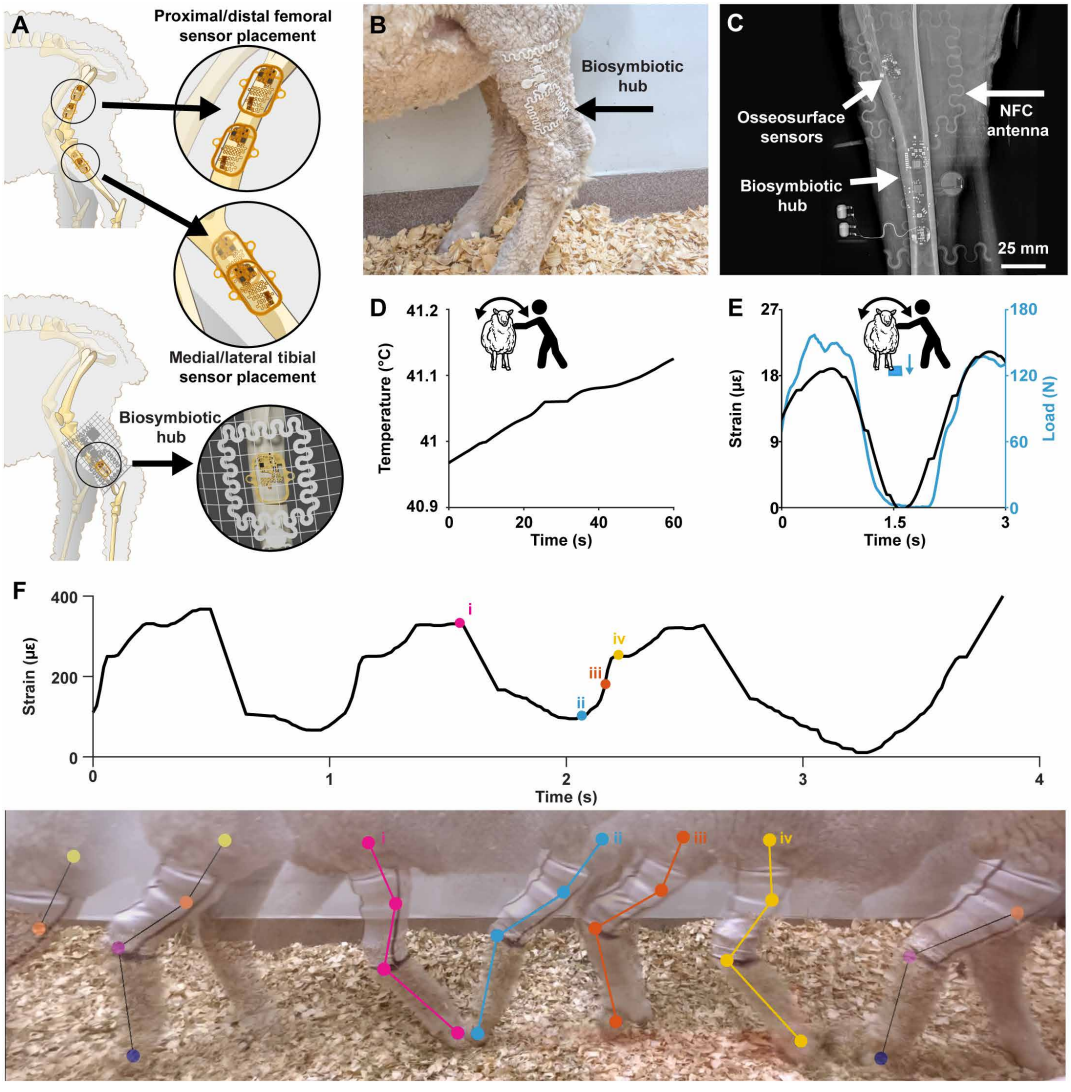

Fig. 5. Large animal studies. (**A**) Top: Diagram showing locations of implanted sensors (medial and lateral rear left tibia, lateral distal and proximal rear left femur) during long-term large animal studies. Top and middle insets show placements of proximal/distal femoral and medial/lateral tibial osseosurface electronics, respectively. Bottom: Placement of wearable over implant site for wireless data collection. (**B**) Photograph showing wearable on sheep tibia. (**C**) Lateral leg radiograph showing location of wearable relative to implant on the medial surface of the tibia. (**D**) Temperature data collected during rocking session. High-resolution temperature sensor shows marked temperature increase over 60-s duration. (**E**) Strain data collected from rocking sheep slowly over 3-s interval. Force plate data during this rocking is shown in blue. (**F**) Graph of bone strain (top) collected from implanted osseosurface sensor via BH during normal gait. Points i to iv are indicated on graph and correlated to four points during time lapse image of gait cycle (below). i, mid-stance; ii, lift-off; iii, mid-swing; iv, touch down.

osseosurface implant. The resulting bone deformation is characterized against a force plate and shown in Fig. 5E.

Implantation surgery has no impact on normal gait, which is illustrated in Fig. 5F. Real-time bone strain is plotted above a composite image of extracted frames from a strain-gait correlation video, movie S1. (isolated frames shown in fig. S15.) Four distinct points during the gait cycle are marked on the strain plot and highlighted in the compound image: (i) mid-stance, (ii) lift-off, (iii) mid-swing, and (iv) touch down. At mid-stance (i), peak strain is experienced as the sheep shifts its weight onto the tibia, and the contralateral limb leaves the ground. The strain profile plateaus then eases as the experimental limb leaves the ground (ii), and the contralateral leg is in mid-stance. This pattern is comparable to strain patterns in sheep tibia previously reported using glued wired strain gauges (*53*). Additional recordings longer than the 4 s shown here are included in fig. S16, demonstrating continuous strain acquisition in vivo during rocking and walking. The ability to capture changes in bone strain profiles facilitates rapid quantification of intervention efficacy, and this level of fidelity represents the most detailed strain characterization in a freely moving large animal model to date.

Chronic monitoring of bone health and fracture recovery in large animal models

Eleven-month-long experiments with six adult sheep demonstrate chronic viability of the device ecosystem. The sheep are implanted with osseosurface electronics on the femur and tibia. Figure 6A (left) shows placement of device and use of resorbable sutures to secure the biointerface during healing. Bone strain is mapped from an axially oriented strain gauge over 4 months post implantation (Fig. 6A, center). At 252 days post-implantation, necropsy is performed, showing osteointegration with the device (Fig. 6A, right). Fibrous capsule formation and local tissue disruption are minimal (additional photographs shown in fig. S17, A and B), and histological staining (fig. S17C) reveals fibrous tissue with blood vessels, fibroblasts, muscle cells, and a minimal number of inflammatory cells, indicating excellent biocompatibility and no detectable interference with the normal wound healing process. Because of its flexible substrate the device conforms readily to the curvature of the bone with no meaningful effects on NFC communication nor power transfer (see fig. S18).

In Fig. 6B, a fluorescent microscopy image shows active bone formation near the site of strain gauge osteointegration at 93 days post-implantation. Osteogenesis is assessed by administration of calcein (*54*). Old bone and recently formed bone above the surface of the strain gauge are visible in the fluorescent microscope image. Osteointegration is also visible in SEM imaging (fig. S19), demonstrating complete integration of the calcium phosphate ceramic (CPC)–coated strain gauge into the underlying bone. This further demonstrates the high biocompatibility of the osseosurface electronics material platform and the general class of flexible implantable devices. Biocompatibility is further demonstrated by osseosurface electronics' robust operational stability over chronic implantation, with no drift in operating frequency (fig. S20A) nor loss of data rate (fig. S20B) despite environmental stresses and bone overgrowth.

Figure 6C shows axial femur strain acquired during rocking of a sheep at increasing number of days post-implantation. Peak-to-peak strain diminishes over months, visible in the reduced magnitude of the femur strain profile at 118 days (27 με) versus 48 days (418 με). This arises from the increasing stiffness of the sensor as osteointegration progresses and the distribution of strain across the increased bone mass. Micro-computed tomography (μCT) analysis (fig. S21) reveals no statistically significant changes in various mechanical and structural characteristics of bone, such as cortical bone volume and the moment of inertia in the implantation site.

The accuracy of osseosurface electronics' strain detection is assessed at 50 days post-implantation using ground reaction force measurements from a force plate and simultaneous strain data from osseosurface electronics (Fig. 6D). The results show high precision and a clear, well-defined linear response of osseosurface electronics in vivo many weeks after implantation.

To assess the impact of the osseosurface device on bone integrity, explanted tibia bones are subject to three-point bending tests, and results are shown in fig. S22. The data show no significant difference (experimental: 133.1 ± 32.22 kg/mm and intact: 135.5 ± 18.02 kg/mm) in whole bone stiffness between implanted and nonimplanted tissues, indicating that osseosurface devices do not compromise bone integrity over chronic time periods. These data combined suggest that device may not need to be recovered and could be part of standard care during complicated reconstruction of fractures or trauma.

To demonstrate utility in a disease model, a sheep fracture model experiment assesses strain as a biomarker for fracture healing. Mid-diaphyseal femoral fractures (shown Fig. 6E, left) are induced in sheep, with osseosurface implants placed adjacent to the fracture. Stainless-steel intramedullary rods provide structural support, internal stability, and promote secondary fracture healing through the course of the 12-week study, which is longer than the reported bone healing time for sheep (*55*). Limited existing literature investigates fracture healing in vivo over extended periods (*56*–*61*); however, current studies rely on indirect assessment and examine deformation of bone hardware rather than bone itself. See table S3 for a more detailed comparison with existing studies that monitor strain in metallic hardware such as plates, fixators, and prostheses.

Figure 6E radiographs show pronounced callus formation between weeks 4 and 6, which coincides with the beginning of weight bearing and is in line with prior work (*55*, *62*). The fracture gap is no longer visible at week 10, with evidence of bone remodeling by week 12. High-resolution radiographs of the bone at week 12, including a lateral view, are shown in fig. S23.

Starting week 5, after sufficient post-surgical recovery, peak-to-peak strain during four-legged walking is recorded by osseosurface electronics, shown Fig. 6F. As noted in literature (*29*, *63*), we measure elevated initial average peak-to-peak strains (82 and 85 με by weeks 5 and 6, respectively), which decrease with osseous callus formation visible in radiographs. Strains reach a minimum (70.8 με) by week 10 and begin increasing during ossification of the callus. To establish a ground truth for strain measurements, weekly assessments of stiffness (see fig. S24) are performed. Resulting data are in line with accepted literature (*64*, *65*).

These results suggest that osseosurface electronics, which are easily integrated into current fracture repair treatment, can provide quantitative assessment. Here, we show a biomarker, the minimum in strain recorded adjacent to a fracture, as a key indicator of bone healing. Bone strains recorded over extended durations correlate well with radiographic analysis, the gold standard for fracture healing assessment (*66*).

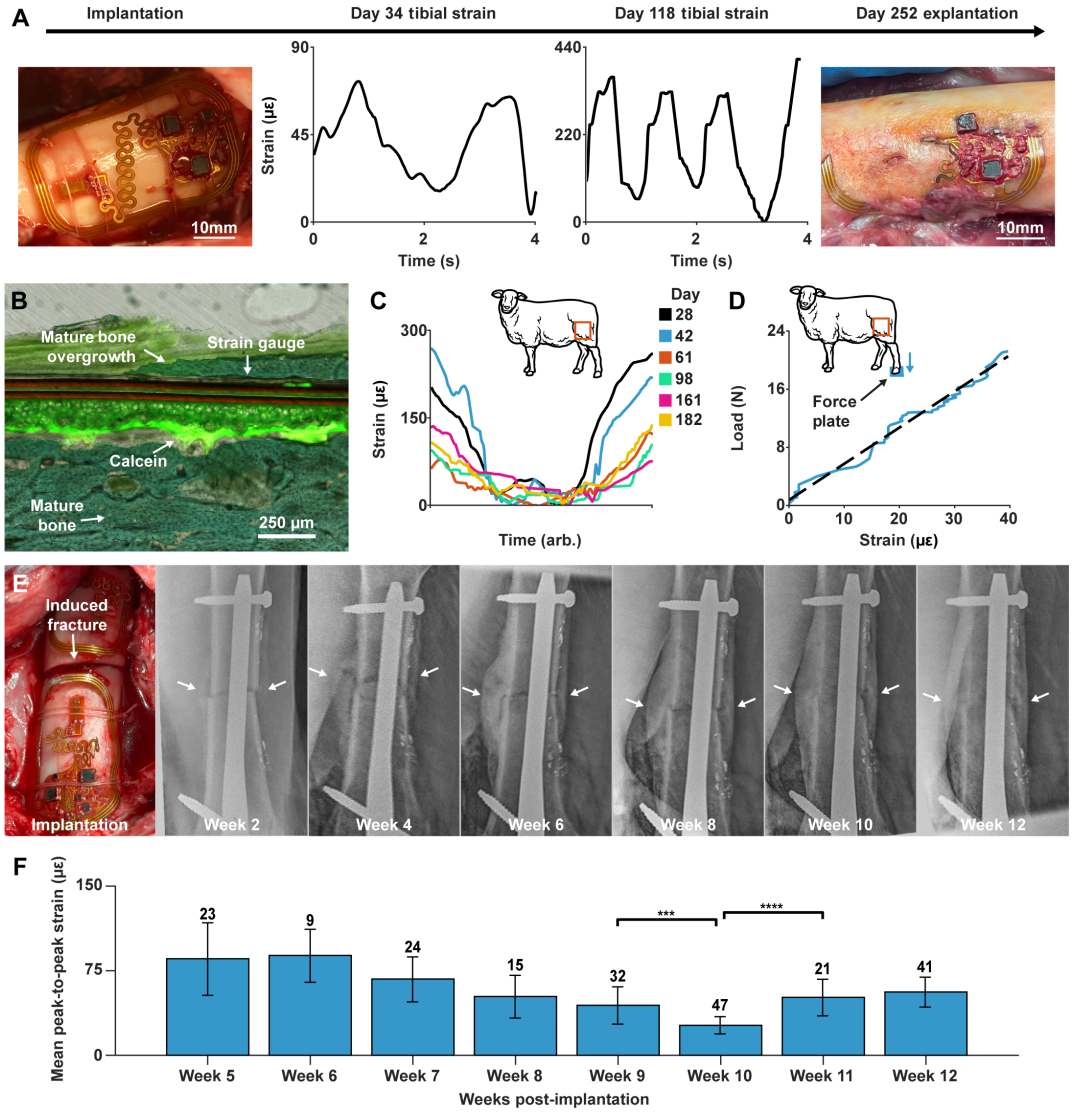

Fig. 6. Chronic monitoring of bone health and fracture recovery in large animal models. (**A**) Photographic image of osseosurface sensor at initial implantation, tibial bone strain data as recorded at 34- and 118-days post-implantation, and the sensor's osteointegration at necropsy as recorded at 252 days post-implantation. (**B**) Fluorescent microscopy image showing osteogenesis at 93 days post-implantation. Calcein was administered 10 and 3 days before analysis to demonstrate ongoing bone formation. (**C**) Strain data extracted from single femur implant over chronic time period. (**D**) Strain sensing precision assessment using simultaneous osseosurface electronics versus gold standard force plate measurements at 50 days post-implantation. (**E**) Biweekly anteroposterior-view radiographs of femoral fracture during recovery. White arrows indicate edges of callus. (**F**) Plot showing weekly average peak-to-peak strain during four-legged walking on a treadmill. Data are shown as means ± SD with value above indicating number of steps analyzed each week. One-way analysis of variance (ANOVA) with multiple comparisons, ***$P < 0.001$ and ****$P < 0.0001$.

DISCUSSION

WBF implantable electronics enable data collection over long timescales, as they are not limited by battery lifetimes. Through WPT methods, such as inductive coupling, enough power is provided for implants to operate continuously with complex sensing and stimulation modalities. However, the power casting devices are often tethered or, when wearable, have large battery supplies (*21*, *22*). Therefore, to provide continuous monitoring, subjects are physically constrained to the tethered reader or must constantly manage the battery life of the wearable.

Here, we introduce a wireless, wearable biosymbiotic hub (BH) capable of transferring power and exchanging data with WBF implantable devices over chronic durations. Far-field power harvesting enables seamless wireless charging of the BH with no modification to daily routines, and no interaction is required from the wearer (*30*–*32*). The use of standardized RF communication protocols enables data exchange and power transfer to any NFC-capable implant. Collecting and relaying data using NFC and BLE maximizes compatibility with existing infrastructure and improves ease of adoption. Experiments showing uninterrupted implant readout and powering for weeks highlight seamless operation of this system architecture. With chronic animal studies, high-fidelity bone strain and temperature characterization in vivo for over 11 months is demonstrated, highlighting the seamless acquisition of key markers of bone health.

Mechanical testing and histological analyses show that osseosurface electronics do not interfere with the wound healing process nor compromise bone integrity, enabling implantation without follow-up surgeries for device removal. Twelve-week-long large animal fracture healing studies show clinical utility and a biomarker of fracture healing and provide a framework for the application of osseosurface electronics in standard fracture care.

Combined, this system architecture offers unprecedented 24/7 access to bone health biomarkers using WBF implantable technologies while allowing patients to move freely and without changes in routine or lifestyle. Autonomous operation allows for uninterrupted data streams of high-fidelity bio signals, allowing physicians to monitor patients remotely, shifting point-of-care from hospitals to homes. In addition, this technology provides a quantitative assessment of fracture healing, improving treatment consistency and reducing healthcare costs when used in conjunction with gold standard radiographic assessment. This technological platform serves as an important demonstration of continuous operation of near-field enabled chronic implants that can transform postoperative monitoring to enable digitally optimized diagnostics and therapeutics. As the theoretical lifetime of WBF thin film implants continues to improve, with existing studies already demonstrating months to years of survival in vivo (*67*, *68*), this platform holds substantial potential for applications beyond simple bone health and fracture recovery analysis. When used with the wearable BH, this device platform enables bone-mounted near-field capable devices to serve as multimodal sensors and actuators for drug delivery (*69*) and other therapeutics, facilitating closed-loop autonomous interventions through seamlessly operating interfaces and achieving a critical step toward the digitally connected body.

METHODS

Study design

This study was designed to evaluate the human translational capacity of osseosurface electronics, assessing feasibility, long-term stability, and practicality through long-term large animal experiments with healthy adult sheep. The second objective was to develop a method of continuous interfacing with WBF fully implantable devices over chronic timescales in freely moving subjects. The final objective was to demonstrate advantages of this device class by targeting physiology, which is now impractical or impossible to assess using traditional technologies.

The study comprised two experimental phases. In phase I, a long-term observational study, devices were implanted in sheep and monitored for 4 to 9 months per animal. This phase observed baseline physiological data, monitored for any signs of infection, and assessed long-term viability of implanted devices. In phase II, osseosurface electronics were used to assess bone healing by direct measurement of bone, not bone hardware, in 12-week long in vivo fracture studies. Randomization and blinding were not applied in this study; all subjects received the same treatment, and data collection and processing were consistent across all subjects.

Sample size was not changed during the study. Data inclusion criteria were established prospectively; only data that could be identified, correlated, and synchronized in video recordings were included in analysis, and any data not meeting these criteria were considered outliers and excluded. Data were collected from rocking and walking each sheep on a weekly basis. Variation in results was anticipated due to physiological differences among subjects.

Wearable and implantable device fabrication

Wearable and implantable electronics were fabricated on a flexible panel structure and sent for external manufacturing. The flexible printed circuit board (PCB) stackup consists of a polyimide substrate (25 μm) between two layers of electroless nickel immersion gold (ENIG)-finished copper (18 μm per layer, 12-μm Cu + 6-μm Au each). Additional polyimide layers (27.5 μm per layer) were used on both sides as solder mask. Devices were depaneled using UV (355 nm) laser ablation (LPKF, ProtoLaser U4) and cleaned via sonication (Vevor, TS391LT) in isopropanol (IPA). Surface mount components were placed and reflowed manually with low-temperature solder paste (Chip Quick, TS391LT).

The contacts of metal-foil strain gauges (Micro Measurements, ED-DY-125BZ-10C/E) were cleaned with soldering flux (Kester, 959 T) and integrated into implantable devices using a soldering iron and low temperature solder paste. After assembly, devices were cleaned once more with IPA and components were then covered with heat cure adhesive (Henkel, Loctite 3621) to secure solder joints and reduce device surface irregularities. Devices were then cured in an oven at 100°C for 10 min. Devices were then washed once more with IPA in a cleanroom environment, treated with silane (A174, Sigma-Aldrich), and encapsulated with two layers of 9-μm parylene-C using a parylene coating system (Parylene P6, Diener electronic GmbH).

Wearable mesh fabrication

High-resolution three-dimensional (3D) scans of subject arms and legs were collected using a handheld 3D scanner (Shining 3D, EinScan Pro HD) and unfolded into 2D maps using open-source 3D creation software (Blender Foundation, Blender). Flexible mesh drawings referenced these 2D maps to ensure accurate wearable device fit and placement. 2D mesh drawings were exported from AutoCAD and imported into a 3D modeling software (Dassault Systèmes, Solidworks) for extrusion. Stereolithography (STL) files were generated from the 3D model and imported into 3D slicing software (Prusa3D, PrusaSlicer) to generate machine code for a 3D printer. A fusion deposition modeling printer (Creality, CR-10s) was outfitted with a custom *x*-axis carriage that housed a direct drive extruder (Creality, Sprite Extruder Pro), hotend, and automatic bed leveling unit (Antclabs, BLTouch). A thermoplastic polyurethane (TPU) filament (NinjaTek, NinjaFlex) was printed at 30 mm/s and 225°C with a bed temperature of 45°C. After printing, segmented sections of the mesh structure were joined by melting TPU material together at junctions to form the completed linear structures.

Wearable device electronics were fabricated in the same manner as implantable device electronics, cleaned with IPA post-assembly, and embedded into the 3D printed TPU mesh. After embedding, the electronics were covered in a transparent, flexible, UV-curable TPU resin (3DMaterials, SuperFlex) dyed white (Alumilite, Resin Dye) to provide wear resistance and protect them from the external environment. The resin-covered electronics were cured with a UV lamp (24 W) for 15 min.

Effect of clothing on biosymbiotic hub data rate

A functional osseosurface implant was epidermally laminated to a subject's lateral brachium, over the deltoid. A serpentine-structured

BH was slid up the arm and placed with the osseosurface implant inside the NFC antenna. Starting with a short sleeve T-shirt, the subject enabled the BH's field over BLE and logged data received from the laminated osseosurface implant for 20 s. The subject changed into a long sleeve T-shirt and the data logging repeated. The experiment was repeated with a conformal athletic shirt and again with a loose-fitting sweatshirt.

Wearable biosymbiotic hub power consumption

A 30-mAh LiPo battery was connected in series with a transimpedance amplifier (LowPowerLab, CurrentRanger) to a BH device with serpentine-structured NFC antenna. An osseosurface implant was placed above the NFC antenna. The BH was powered on and autonomously switched into low-power idle. Connection with the BH was then made over BLE using a cell phone, and last, the reader field was switched on. An oscilloscope (Siglent, SDS1202X-E) monitored the voltage output from the transimpedance circuit.

Wearable power transfer and data rate through tissue characterization

Two osseosurface implants were adhered to a sheep femur, one with full functionality and all components populated and the other with only power harvesting components to assess power transfer of the BH through tissue. Increasing thicknesses of tissue phantom (porcine tissue) were placed above the osseosurface. A 217-ohm load was connected to the power harvesting osseosurface implant, and the voltage across the load was monitored using a multimeter (AstroAI, AM33B). A BH with 18AWG wire-wound four-turn circular coil antenna was placed above the functional osseosurface implant, the hub's electromagnetic field was switched on via BLE connection, and data from the implant was collected by the BH and transmitted over BLE to a logging computer for 20 s. The hub was switched off, positioned above the power harvesting osseosurface implant, and the hub's field was re-enabled. The voltage from the multimeter was recorded.

Wearable electromagnetic field output characterization

Two wearable BHs were adhered using Kapton tape to paper grids with 1-cm gridlines. One BH used an 18AWG wire-wound four-turn circular coil antenna, and the other used a planar serpentine-structured flexPCB antenna. A characteristic osseosurface implant antenna (osseosurface device with only matching capacitance and power rectification circuitry) was attached to a 217-ohm load and adhered to a microscope slide using Kapton tape. The center of the osseosurface antenna was marked onto the microscope slide. The position of the center of the osseosurface implant antenna was moved to each 1-cm grid point within and around the BH antenna. Voltage harvested by the osseosurface antenna was recorded using a multimeter (AstroAI, AM33B). The antenna was raised 15 mm using plastic spacers, and measurements were repeated at 15, 30, and 45 mm.

Stretchability of biosymbiotic hub

A functional BH with serpentine-structured NFC antenna was assembled with the TPU mesh laid flat. Both ends of the mesh were clamped evenly into a purpose-designed stretching stage and slack removed from the system such that the mesh was taut without stretch. An osseosurface implant with only power harvesting components was attached to a 217-ohm load. A multimeter (AstroAI, AM33B) monitored the voltage across the load. The electromagnetic field of the BH was enabled over BLE, and the voltage was measured by the multimeter. The field was switched off, and the stretching stage was set to induce a 10% strain across the length of the mesh. The BH field was re-enabled, and harvested voltage was again measured. This was repeated at 20, 30, and 40% strain.

Wearable power transfer analysis with three antennas

Three flexPCB antennas with varying physical dimensions and numbers of turns were tuned to 13.56 MHz and adhered to microscope slides using Kapton tape. Using the same setup from the wearable electromagnetic field output characterization, the flexPCB antennas were placed into the center of the BH with serpentine-structured flexPCB antenna at 0-mm height. A variable load board was connected to each antenna and a load sweep from 12 to 9800 ohm was performed, with voltages recorded by multimeter (AstroAI, AM33B).

Human wearability experiments

Using 3D scans taken of a subject's arm, a wearable BH with serpentine-structured flexPCB antenna was assembled. A parylene-encapsulated osseosurface device was epidermally laminated to the wearer's right arm, superficial to the deltoid using transparent medical adhesive, which was replaced every few days as the adhesives failed due to sweat, external forces, and skin turnover. When powered, this osseosurface device incremented a two-byte integer counter at 1-ms intervals, storing each value into an array. After incrementing 127 times (two-byte integer $\times$ 127 = 254 bytes total), the device recorded ambient temperature data (two bytes) and transferred the array and temperature data onto the onboard NFC tag (256-byte buffer) to be retrieved by the wearable BH.

The wearable device was slid up the arm, and the NFC antenna was aligned over the laminated osseosurface device. The wearable BH was powered on, where it autonomously entered a low-power sleep mode with BLE remaining active. The subject was instructed to wear the device continuously for a 2-week period and perform regular daily activities. A logging device was connected to the wearable BH via BLE at regular intervals. Upon connection with the logger, the wearable BH woke from low-power sleep, collected battery voltage data, enabled the NFC reader field to power the epidermally laminated osseosurface device, and aggregated data acquired via NFC from the osseosurface device over a 20-s period. The data were sent over BLE to the logging device, which then disconnected after receiving all data recorded over the 20-s period. After disconnection from the logger, the wearable BH disabled the NFC reader field and returned to low power sleep mode.

A commercial 915-MHz power caster (Powercast, TX91501B) was placed at the subject's office desk. The wearable was recharged during the work week, while the subject was at their desk. The wearable device was not recharged during the weekend (days 2, 3, 8, and 9), demonstrating the device's ability to operate when consistent charging is not reliable.

Stiffness of mesh structure versus commercial smartwatch band

A commercial soft, silicone smartwatch band was clamped at both ends into a custom, 3D printed stretching stage. The band was clamped to set initial unstretched length to 100 mm. The stretching stage used a 5 kg of load cell (Degraw, 050HX) and load cell amplifier

(SparkFun, HX711) to measure bulk strain profiles during displacement. The band was manually stretched to 10 and 20% displacement, and load cell measurements were recorded at each displacement. This process was repeated for a 3D printed biosymbiotic mesh with a similar width and initial length.

Gold standard strain comparison, gain, and biasing circuit validation

An intact femur was kept hydrated in phosphate-buffered saline (PBS)–soaked gauze during the preparation of the experiments. The bottom of the high precision 1 kilohm of metal-foil strain gauge (Micro-Measurements, ED-DY-125BZ-10C/E) of an osseosurface device was glued to the anterior diaphyseal surface of an intact sheep femur using a cyanoacrylate-based adhesive (Micro-Measurements, M-Bond 200). An additional, hard-wired, uniaxial strain gauge (ED-DY-125BZ-10C/E, Micro-Measurements) was directly glued on top of the osseosurface strain gauge. Great care was taken to overlap the two sensing elements with the gauges in the axial direction of the femur. The rigid glue interface and any misalignment would induce variability in sensor readings and contribute to error estimation. The femoral condyles were potted in fixture using a low-melting point alloy (Cerrobend, Scottsdale Tool, AZ). The bone was loaded in cantilever bending using a servo-hydraulic MTS 810 (MTS Systems, Eden Prairie, MN). The bone was positioned so that the loading pin was perpendicular the femoral head, applying tension to the anterior diaphyseal surface.

For gold standard hard-wired comparison, a ramp function was applied at a load rate of 20 N/s to a peak load of 200 N. The force was held for 10 s and then unloaded at −20 N/s. For gain and biasing validation, a ramp function was applied at a load rate of 40 N/s to a peak load of 200 N. The osseosurface implant gain was set to 200 V/V, bias was adjusted to mid-ADC range, and the device was powered via WPT from the 20-cm circular antenna used during long-term large animal studies.

During loading, strain measurements were collected from both the osseosurface device and the wired strain gauge. The loading parameters were repeated with the osseosurface device at 10, 100, and 200 gain. For biasing quantification, the bone was placed under the same loading conditions at different biasing modalities.

This was repeated for digipot values, including values which would induce signal clipping at maximum and minimum ADC values, demonstrating the ability to wirelessly adjust for surgically induced prestrain. Bias adjustment units are digital values for setting the 8-bit digital potentiometer. Given that we use a 5 kΩ of 8-bit digital potentiometer, a single value change up or down equates to a potentiometer resistance change of approximately (5000 ohm/2^8 =) 19.5 ohm up or down, respectively.

Thermography versus gold standard thermocouple

An osseosurface implant was coated in 18-μm parylene-C using a parylene coating system (Diener Electronic, Parylene P6) to waterproof it. The waterproofed implant was placed into a glass jar of distilled water. The jar was placed onto a hotplate and heated to 44°C, as measured by a commercial thermocouple. The hotplate was switched off, and the water bath was allowed to cool. Readings from the commercial thermocouple were recorded every minute. Thermography data were retrieved every minute from the osseosurface implant using a high-frequency (HF) long-range radio-frequency identification (RFID) reader (Feig Electronic GmbH, ID LR2500).

Animal studies

All animal studies were performed following an Institutional Animal Care and Use Committee (IACUC) approved protocol. Six adult sheep in total were used (three male and three female; weights, 49 to 81 kg) for long-term in vivo data collection. After device encapsulation with 18-μm parylene-C, CPC particles were adhered to osseosurface implant strain gauges using ISO10993 biocompatibility-compliant epoxy adhesive (Master Bond Polymer System, EP42HT-2Med). Implanted devices were sterilized using ethylene oxide. One day before surgery, 1 μl of transforming growth factor–β (concentration of 0.3 μg/μl) was placed directly on the CPC-coated strain gauge. Sheep were anesthetized using Ketamine and isoflurane prior to surgery. An 8-cm incision was made over the lateral thigh of the left hindlimb. The iliotibial band was incised, and the interval between the quadriceps and hamstrings was developed to expose the lateral surface of the femur. Two devices were placed at the midpoint of the bone diaphysis, spaced approximately 5-cm apart with strain gauges oriented axially along the femur. The devices were secured in place using circumferentially tied 2-0 Vicryl (Ethicon Inc., J269H). The incision was closed in a layered fashion. Next, a 6-cm incision was made on the medial side of the leg to expose the proximal left tibia. Subperiosteal dissection was used to expose the lateral surfaces of the tibia. One device was placed on the medial surface and one on the lateral surface of the tibia with the strain gauges oriented axially. Gauges were secured using circumferencially tied 2-0 Vicryl before the incision was closed. For each device, one suture was threaded through the tabs on either side to minimize implant migration, and two sutures were used to secure the strain gauge. After wound closure, device gain was set to 200×, and device biasing was adjusted to center the baseline strain at half the maximum ADC value. Data collection began approximately 3 weeks post-implantation to allow for wound healing and osteointegration of the strain gauges. Subcutaneous injections of calcein (C-0875, Sigma-Aldrich) were administered 10 and 3 days before euthanasia at a dose of 20 mg/kg for visualization of active bone growth near the osseosurface device interface.

Osseosurface device placement is shown in Fig. 5A. For 11-month long large animal studies (data shown in Figs. 5, D to F and 6, A to C, and figs. S13-S18, S20, S21, S24, and S25), devices were implanted in all four locations. For 12-week long fracture recovery studies (data shown in Fig. 6, E and F, and figs. S22 and S23), only the two distal/proximal femoral placements were used.

Radiographs

In vivo radiographic images were taken using a Stalo ultra high-definition x-ray acquisition station (Universal Imaging, Stalo Series Canon). The station is equipped with a wireless detector (Canon, CXDI-801C Wireless Detector) and a battery-powered portable x-ray generator (Ecoray, Ultra 9020BT). X-ray images of sheep were taken in the anterior-posterior and lateral-medial views using 84 kV_p and 2.5 mAs. Digital Imaging and Communications in Medicine (DICOM) images were viewed and exported using the MicroDicom software (MicroDicom Ltd.).

Long-term large animal model implant data collection

A HF long-range RFID reader (Feig Electronic GmbH, ID LR2500) was connected to three-turn circular antenna with a diameter of 20 cm and adjustable antenna tuning circuit. The coil antenna was embedded into a 3D printed polylactic acid (PLA) (OVERTURE, 1.75-mm PLA) housing to provide rigidity and maintain structural

integrity. The tuning circuit was adjusted to match to 50 ohm at 13.56 MHz. Large animal subjects (sheep) were led onto a purpose-built treadmill and a camera (1920 × 1080, 60 frames/s, iPhone 14 Pro Max) was placed sagittally to capture movement of all four limbs. For gait recording experiments, the treadmill was activated, and subjects were able to walk for 2 min at 2.6 km/hour for each osseosurface device. For nongait strain recording sessions, the treadmill was left off, and animals were gently rocked by researchers at 0.5 Hz for 2-min intervals for each osseosurface device. During rocking, the experimental limb was on a force plate (ATMI, AccuGait-Optimized). During data collection, the field output power was set between 5.75 and 6.25 W, and the coil antenna was placed against the subject over the implant site. Raw hex data were collected from each implant via HF Reader control software (Feig Electronic GmbH, ID ISOStart+ V11) scripts at approximately 84 Hz. The data were extracted and formatted using MATLAB. Implant biasing and gain were adjusted as needed.

Implant biasing and gain adjustment during animal studies

The strain sensing circuit was implemented using a Wheatstone bridge configuration, with two 1 kilohm of 0.1% resistors (Vishay/Dale, TNPW02011K00BEED) forming one half of the bridge, a 5 kilohm of digital potentiometer (Microchip Technology, MCP4561) in parallel with a 2.2 kilohm of 5% resistor and a high precision 1 kilohm of metal-foil strain gauge (Micro Measurements, ED-DY-125BZ-10C/E) forming the other half. To adjust biasing of the bridge, values stored in the NFC tag are read upon boot by the microcontroller and loaded into the digital potentiometer via I^2C communication. For gain adjustment of the output stage, the low-power, high-precision instrumentation amplifier (Maxim Integrated, MAX41400) uses two digital input pins to adjust gain. These pins are connected to general purpose input-outputs (GPIOs) on the microcontroller, which are set upon boot using values retrieved from the NFC tag.

The gain of individual implants was adjusted as necessary to maintain significant strain signal amplitude without voltage clipping. Wheatstone bridge biasing was adjusted to account for pre-strain of the strain gauge introduced during surgical implantation and subsequent wound healing process.

Wireless strain acquisition using biosymbiotic hub on freely moving large animal model

Axial tibia strain data from an osseosurface implant was collected over NFC by BH with circular coil NFC antenna, transmitted over BLE to a logging device, and time-synchronized with a video of the sheep walking (movie S1). Neural network analysis was used to plot trajectories of the hoof, ankle, osseosurface implant/wearable, and stifle, which are marked with blue, purple, orange, and yellow, respectively.

Computed tomography

Bones were explanted and maintained in PBS-soaked gauze to prevent dehydration. Bones were imaged using an Inveon μCT scanner (Siemens, Malvern, PA) with an effective pixel size of 52.75 μm (voltage: 80 kV; current: 500 μA; exposure, 200 ms). DICOM images were analyzed using DragonFly version 2022.2 (Object Research Systems) and BoneJ/ImageJ. Parameters measured in the implant site included cortical bone volume (mm^3), second moment of inertia around the minor axis (I_{Min}) (mm^4), and the second moment of inertia around the major axis (I_{Max}) (mm^4).

Histology and scanning electron microscopy

Following euthanasia, the soft tissue between the implant muscle was carefully excised. The tissue was fixed in 10% neutral buffer formalin (NBF), embedded in paraffin block, cut in 5 –μm-thick sections, and stained using hematoxylin and eosin. Femurs and tibias were cut proximal and distal to the implant location for hard tissue histology and electron microscopy. Bones were left in a 10% NBF solution for 24 hours followed by increasing solutions of ethanol (70, 80, 90, 95, and 100%) for 24 hours each, in a xylene solution for 24 hours to defat the tissue and returned to 100% ethanol after. Bones were embedded in polymethyl methacrylate (PMMA) using the Polysciences PMMA kit (Polysciences Inc., Warrington, PA) and mounted on a slide for cross sectional slicing with a diamond saw (Bronwill Scientific, Rochester, NY). Slices included a transverse and sagittal cuts for scanning electron microscopy (SEM) and histology, respectively. Histology slides were ground to one to three cell layers thick and stained using the Villanueva's mineralized bone stain (MIBS, Polysciences Inc., Warrington, PA.). Stained sections were imaged in a Leica DMI6000 motorized inverted microscope under brightfield and fluorescence imaging. The SEM PMMA embedded samples were cut 3-cm thick and were polished for SEM imaging. Samples were coated using a Hummer 6.3 gold sputter machine (Anatech, USA, Sparks, NV) and imaged using an Inpec-S Scanning Electron Microscope (FEI Company, USA). Backscattered electron (BSEM) images were taken at ×440 magnification to observe strain gauge attachment to the bone.

Mechanical characterization of bone stiffness

Mechanical characterization of experimental bone stiffness was performed using a servo-hydraulic MTS (MTS Systems Corporation, Series 810). The experimental and contralateral intact bones were explanted and cleaned of soft tissue. Tibias underwent a three-point bending. A ramp function was applied with a load rate of 19.66 N/s to peak load at 196.6 N. A load versus deformation plot was made, and the slope of the linear portion was used to calculate the mechanical stiffness of the specimen.

Sheep model fracture healing experiments

All animal studies were performed following an IACUC-approved protocol. Three adult sheep were used to study fracture healing, with characteristic data shown in Fig. 6E and F. Implanted devices were sterilized using ethylene oxide. Sheep were anesthetized using ketamine and isoflurane before surgery. An 8-cm incision was made over the lateral thigh of the left hindlimb. The iliotibial band was incised, and the interval between the quadriceps and hamstrings was developed to expose the lateral surface of the femur. A mid-diaphyseal osteotomy is created using a sagittal saw. Stainless-steel Zimmer humeral intramedullary nails, 8 mm-diameter, were modified for use in ovine femoral defect model (*70*). The nail is inserted into the femur in a retrograde fashion, and a surgical placement guide is used to place an interlocking screw proximal and distal to the osteotomy site to obtain axial and torsional stability. Osseosurface devices were placed at both sides of the osteotomy site with strain gauges oriented axially along the femur. The devices were secured in place using circumferentially tied 2-0 Vicryl. Transforming growth factor–β was not used in fracture healing experiments. The incision was closed in a layered fashion. Data collection began approximately 5 weeks post-implantation to allow for wound healing and osteointegration of the strain gauges.

In vivo bone stiffness assessment

Animals were gently rocked by researchers at 0.5 Hz for 2-min intervals, while the experimental limb was on a force plate (ATMI, AccuGait-Optimized). Great care was taken to verify that the experimental limb was perpendicular to the force plate and prevent bending of the joint. Strain data was collected from osseosurface electronics using the same setup as during 11-month-long large animal experiments. Strain and force measurements were synchronized using timestamped video recordings and used to calculate stiffness. Bone stiffness was calculated using the linear slope of the load (N) versus strain (με) curve.

Statistical analysis

All statistical analyses were carried out in Graphpad Prism (v.10.2.3). Weekly peak-to-peak strain and stiffness values were obtained from walking and rocking sessions in the same day. An ordinary one-way analysis of variance (ANOVA) was performed to compare values across each week. All bar charts are shown as mean ± SD with the number of steps and peaks analyzed in the weekly walking and stiffness data, respectively. Statistical significance is demonstrated as $*P < 0.05$, $**P < 0.01$, $***P < 0.001$, and $****P < 0.0001$.

Supplementary Materials

The PDF file includes:

Figs. S1 to S24
Tables S1 to S3
Legend for movie S1

Other Supplementary Material for this manuscript includes the following:

Movie S1

REFERENCES AND NOTES

1. M. A. De Georgia, F. Kaffashi, F. J. Jacono, K. A. Loparo, Information technology in critical care: Review of monitoring and data acquisition systems for patient care and research. *ScientificWorldJournal* **2015**, 727694 (2015).
2. M. M. El Khatib, G. Ahmed, Management of artificial intelligence enabled smart wearable devices for early diagnosis and continuous monitoring of CVDS. *Int. J. Innov. Technol. Explor. Eng.* **9**, 1211–1215 (2019).
3. R. Rebelo, A. I. Barbosa, D. Caballero, I. K. Kwon, J. M. Oliveira, S. C. Kundu, R. L. Reis, V. M. Correlo, 3D biosensors in advanced medical diagnostics of high mortality diseases. *Biosens. Bioelectron.* **130**, 20–39 (2019).
4. T. R. Ray, J. Choi, A. J. Bandodkar, S. Krishnan, P. Gutruf, L. Tian, R. Ghaffari, J. A. Rogers, Bio-integrated wearable systems: A comprehensive review. *Chem. Rev.* **119**, 5461–5533 (2019).
5. Y. Song, J. Min, W. Gao, Wearable and implantable electronics: Moving toward precision therapy. *ACS Nano* **13**, 12280–12286 (2019).
6. M. Joshi, H. Ashrafian, L. Aufegger, S. Khan, S. Arora, G. Cooke, A. Darzi, Wearable sensors to improve detection of patient deterioration. *Expert Rev. Med. Devices* **16**, 145–154 (2019).
7. E. Rovini, C. Maremmani, F. Cavallo, How wearable sensors can support parkinson's disease diagnosis and treatment: A systematic review. *Front. Neurosci.* **11**, 555 (2017).
8. J. P. L. Leenen, C. Leerentveld, J. D. van Dijk, H. L. van Westreenen, L. Schoonhoven, G. A. Patijn, Current evidence for continuous vital signs monitoring by wearable wireless devices in hospitalized adults: Systematic review. *J. Med. Internet Res.* **22**, e18636 (2020).
9. T. Lu, S. Ji, W. Jin, Q. Yang, Q. Luo, T.-L. Ren, Biocompatible and long-term monitoring strategies of wearable, ingestible and implantable biosensors: Reform the next generation healthcare. *Sensors* **23**, 2991 (2023).
10. T. Niederhauser, A. Haeberlin, T. Marisa, D. Mattle, R. Abächerli, J. Goette, M. Jacomet, R. Vogel, An optimized lead system for long-term esophageal electrocardiography. *Physiol. Meas.* **35**, 517–532 (2014).
11. R. Haessler, F. Brandl, M. Zeller, J. Briegel, K. Peter, Continuous intra-arterial oximetry, pulse oximetry, and co-oximetry during cardiac surgery. *J. Cardiothorac. Vasc. Anesth.* **6**, 668–673 (1992).
12. S. R. Khan, S. K. Pavuluri, G. Cummins, M. P. Y. Desmulliez, Wireless power transfer techniques for implantable medical devices: A review. *Sensors* **20**, 3487 (2020).
13. K. Agarwal, R. Jegadeesan, Y. X. Guo, N. V. Thakor, Wireless power transfer strategies for implantable bioelectronics. *IEEE Rev. Biomed. Eng.* **10**, 136–161 (2017).
14. S. Y. Yang, V. Sencadas, S. S. You, N. Z. X. Jia, S. S. Srinivasan, H. W. Huang, A. E. Ahmed, J. Y. Liang, G. Traverso, Powering implantable and ingestible electronics. *Adv. Funct. Mater.* **31**, 2009289 (2021).
15. H. Basaeri, D. B. Christensen, S. Roundy, A review of acoustic power transfer for bio-medical implants. *Smart Mater. Struct.* **25**, 123001 (2016).
16. V. Nair, A. N. Dalrymple, Z. Yu, G. Balakrishnan, C. J. Bettinger, D. J. Weber, K. Yang, J. T. Robinson, Miniature battery-free bioelectronics. *Science* **382**, eabn4732 (2023).
17. A. Bhatia, J. Hanna, T. Stuart, K. A. Kasper, D. M. Clausen, P. Gutruf, Wireless battery-free and fully implantable organ interfaces. *Chem. Rev.* **124**, 2205–2280 (2024).
18. L. Cai, P. Gutruf, Soft, wireless and subdermally implantable recording and neuromodulation tools. *J. Neural Eng.* **18**, 041001 (2021).
19. D. K. Piech, B. C. Johnson, K. Shen, M. M. Ghanbari, K. Y. Li, R. M. Neely, J. E. Kay, J. M. Carmena, M. M. Maharbiz, R. Muller, A wireless millimetre-scale implantable neural stimulator with ultrasonically powered bidirectional communication. *Nat. Biomed. Eng.* **4**, 207–222 (2020).
20. A. Khalifa, S. Lee, A. C. Molnar, S. Cash, Injectable wireless microdevices: Challenges and opportunities. *Bioelectron. Med.* **7**, 19 (2021).
21. T. J. Oxley, P. E. Yoo, G. S. Rind, S. M. Ronayne, C. M. S. Lee, C. Bird, V. Hampshire, R. P. Sharma, A. Morokoff, D. L. Williams, C. MacIsaac, M. E. Howard, L. Irving, I. Vrljic, C. Williams, S. E. John, F. Weissenborn, M. Dazenko, A. H. Balabanski, D. Friedenberg, A. N. Burkitt, Y. T. Wong, K. J. Drummond, P. Desmond, D. Weber, T. Denison, L. R. Hochberg, S. Mathers, T. J. O'Brien, C. N. May, J. Mocco, D. B. Grayden, B. C. V. Campbell, P. Mitchell, N. L. Opie, Motor neuroprosthesis implanted with neurointerventional surgery improves capacity for activities of daily living tasks in severe paralysis: First in-human experience. *J. Neurointerv. Surg.* **13**, 102–108 (2021).
22. H. Lorach, A. Galvez, V. Spagnolo, F. Martel, S. Karakas, N. Intering, M. Vat, O. Faivre, C. Harte, S. Komi, J. Ravier, T. Collin, L. Coquoz, I. Sakr, E. Baaklini, S. D. Hernandez-Charpak, G. Dumont, R. Buschman, N. Buse, T. Denison, I. van Nes, L. Asboth, A. Watrin, L. Struber, F. Sauter-Starace, L. Langar, V. Auboiroux, S. Carda, S. Chabardes, T. Aksenova, R. Demesmaeker, G. Charvet, J. Bloch, G. Courtine, Walking naturally after spinal cord injury using a brain–spine interface. *Nature* **618**, 126–133 (2023).
23. O. Padron, C. Hanson, R. McCrery, S. de Wachter, B. Blok, A. Lucioni, J. Mangel, D. Vrijens, M. Smit, J. V. Boatman, V. Mark, A. Yeh, A. Hougham, S. Siegel, Treatment of Urinary Urgency Incontinence (UUI) with an ultra-miniaturized sacral nerve modulation (SNM) System: Preliminary outcomes of the Sans-UUI Study. *J. Urol.* **206**, 101719 (2021).
24. F. T. Alrashdan, J. C. Chen, A. Singer, B. W. Avants, K. Yang, J. T. Robinson, Wearable wireless power systems for "ME-BIT" magnetoelectric-powered bio implants. *J. Neural Eng.* **18**, 045011 (2021).
25. N. Anabtawi, S. Freeman, R. Ferzli, A fully implantable, NFC enabled, continuous interstitial glucose monitor, in *the Third IEEE EMBS International Conference on Biomedical and Health Informatics (BHI)* (IEEE, 2016), pp. 612–615.
26. M. Zhumayeva, K. Dautov, M. Hashmi, G. Nauryzbayev, Wireless energy and information transfer in WBAN: A comprehensive state-of-the-art review. *Alex. Eng. J.* **85**, 261–285 (2023).
27. S. Cho, I. Ensari, C. Weng, M. G. Kahn, K. Natarajan, Factors affecting the quality of person-generated wearable device data and associated challenges: Rapid systematic review. *JMIR Mhealth Uhealth* **9**, e20738 (2021).
28. N. Alshurafa, J. A. Eastwood, S. Nyamathi, J. J. Liu, W. Xu, H. Ghasemzadeh, M. Pourhomayoun, M. Sarrafzadeh, Improving compliance in remote healthcare systems through smartphone battery optimization. *IEEE J. Biomed. Health Inform.* **19**, 57–63 (2015).
29. L. Cai, A. Burton, D. A. Gonzales, K. A. Kasper, A. Azami, R. Peralta, M. Johnson, J. A. Bakall, E. Barron Villalobos, E. C. Ross, J. A. Szivek, D. S. Margolis, P. Gutruf, E. B. Villalobos, E. C. Ross, J. A. Szivek, D. S. Margolis, P. Gutruf, Osseosurface electronics-thin, wireless, battery-free and multimodal musculoskeletal biointerfaces. *Nat. Commun.* **12**, 6707 (2021).
30. T. Stuart, K. A. Kasper, I. C. Iwerunmor, D. T. McGuire, R. Peralta, J. Hanna, M. Johnson, M. Farley, T. LaMantia, P. Udorvich, P. Gutruf, Biosymbiotic, personalized, and digitally manufactured wireless devices for indefinite collection of high-fidelity biosignals. *Sci. Adv.* **7**, eabj3269 (2021).
31. T. Stuart, X. Yin, S. J. Chen, M. Farley, D. T. McGuire, N. Reddy, R. Thien, S. DiMatteo, C. Fumeaux, P. Gutruf, Context-aware electromagnetic design for continuously wearable biosymbiotic devices. *Biosens. Bioelectron.* **228**, 115218 (2023).
32. T. Stuart, M. Farley, J. Amato, R. Thien, J. Hanna, A. Bhatia, D. M. Clausen, P. Gutruf, Biosymbiotic platform for chronic long-range monitoring of biosignals in limited resource settings. *Proc. Natl. Acad. Sci. U.S.A.* **120**, e2307952120 (2023).
33. X. Yin, T. Stuart, S. J. Chen, M. Farley, P. Gutruf, C. Fumeaux, Biosymbiotic 3D-printed planar inverted-F antenna. *IEEE Trans. Antennas Propag.* **72**, 412–423 (2023).
34. Y. Zhang, H. Fu, Y. Su, S. Xu, H. Cheng, J. A. Fan, K.-C. Hwang, J. A. Rogers, Y. Huang, Mechanics of ultra-stretchable self-similar serpentine interconnects. *Acta Mater.* **61**, 7816–7827 (2013).

35. S. D. Barman, A. W. Reza, N. Kumar, M. E. Karim, A. B. Munir, Wireless powering by magnetic resonant coupling: Recent trends in wireless power transfer system and its applications. *Renew. Sustain. Energy Rev.* **51**, 1525–1552 (2015).
36. Consumer and Governmental Affairs Bureau, Federal Communications Commission, *Wireless Devices and Health Concerns* (2020); www.fcc.gov/sites/default/files/wireless_devices_and_health_concerns.pdf.
37. International Commission on Non-Ionizing Radiation Protection (ICNIRP), Guidelines for Limiting Exposure to Electromagnetic Fields (100 kHz to 300 GHz). *Health Phys.* **118**, 483–524 (2020).
38. International Organization for Standardization, Cards and security devices for personal identification (ISO/IEC 15693-1:2018, 2018).
39. R. Martinek, M. Ladrova, M. Sidikova, R. Jaros, K. Behbehani, R. Kahankova, A. Kawala-Sterniuk, Advanced bioelectrical signal processing methods: Past, present and future approach-Part II: Brain signals. *Sensors* **21**, 6343 (2021).
40. A. Burton, S. N. Obaid, A. Vázquez-Guardado, M. B. Schmit, T. Stuart, L. Cai, Z. Chen, I. Kandela, C. R. Haney, E. A. Waters, H. Cai, J. A. Rogers, L. Lu, P. Gutruf, Wireless, battery-free subdermally implantable photometry systems for chronic recording of neural dynamics. *Proc. Natl. Acad. Sci. U.S.A.* **117**, 2835–2845 (2020).
41. J. Ausra, M. Wu, X. Zhang, A. Vázquez-Guardado, P. Skelton, R. Peralta, R. Avila, T. Murickan, C. R. Haney, Y. Huang, J. A. Rogers, Y. Kozorovitskiy, P. Gutruf, Wireless, battery-free, subdermally implantable platforms for transcranial and long-range optogenetics in freely moving animals. *Proc. Natl. Acad. Sci. U.S.A.* **118**, e2025775118 (2021).
42. P. Gutruf, R. T. Yin, K. B. Lee, J. Ausra, J. A. Brennan, Y. Qiao, Z. Xie, R. Peralta, O. Talarico, A. Murillo, S. W. Chen, J. P. Leshock, C. R. Haney, E. A. Waters, C. Zhang, H. Luan, Y. Huang, G. Trachiotis, I. R. Efimov, J. A. Rogers, Wireless, battery-free, fully implantable multimodal and multisite pacemakers for applications in small animal models. *Nat. Commun.* **10**, 5742 (2019).
43. A. Burton, S. M. Won, A. K. Sohrabi, T. Stuart, A. Amirhossein, J. U. Kim, Y. Park, A. Gabros, J. A. Rogers, F. Vitale, A. G. Richardson, P. Gutruf, Wireless, battery-free, and fully implantable electrical neurostimulation in freely moving rodents. *Microsyst. Nanoeng.* **7**, 62 (2021).
44. G. Shin, M. H. Jarrahi, Y. Fei, A. Karami, N. Gafinowitz, A. Byun, X. Lu, Wearable activity trackers, accuracy, adoption, acceptance and health impact: A systematic literature review. *J. Biomed. Inform.* **93**, 103153 (2019).
45. B. A. Rabkin, J. A. Szivek, J. E. Schonfeld, B. P. Halloran, Long-term measurement of bone strain in vivo: The rat tibia. *J. Biomed. Mater. Res.* **58**, 277–281 (2001).
46. C. T. Rubin, L. E. Lanyon, Dynamic strain similarity in vertebrates; an alternative to allometric limb bone scaling. *J. Theor. Biol.* **107**, 321–327 (1984).
47. R. Steck, C. Gatzka, E. Schneider, P. Niederer, M. L. Knothe Tate, Measurement of bone surface strains on the sheep metacarpus in vivo and ex vivo. *Vet. Comp. Orthop. Traumatol.* **16**, 38–43 (2003).
48. P. Cabahug-Zuckerman, C. Liu, A. B. Castillo, *Cells involved in mechanotransduction including mesenchymal stem cells* (Elsevier Inc., 2020); https://www.sciencedirect.com/science/article/pii/B9780128012383112097.
49. S. C. Cowin, Ed., in *Bone Mechanics Handbook* (CRC Press, 2001), pp. 8–1 to 8–35.
50. N. Verma, I. Haji-Abolhassani, S. Ganesh, J. Vera-Aguilera, J. Paludo, R. Heitz, S. N. Markovic, K. Kulig, A. Ghoreyshi, A Novel wearable device for continuous temperature monitoring & fever detection. *IEEE J. Transl. Eng. Health Med.* **9**, 2700407 (2021).
51. A. Banstola, J. N. J. Reynolds, The sheep as a large animal model for the investigation and treatment of human disorders. *Biology* **11**, 1251 (2022).
52. K. E. Renner, A. T. Peebles, J. J. Socha, R. M. Queen, The impact of sampling frequency on ground reaction force variables. *J. Biomech.* **135**, 111034 (2022).
53. L. E. Lanyon, R. N. Smith, Measurements of bone strain in the walking animal. *Res. Vet. Sci.* **10**, 93–94 (1969).
54. L. Sun, H. C. Blair, Y. Peng, N. Zaidi, O. A. Adebanjo, X. B. Wu, X. Y. Wu, J. Iqbal, S. Epstein, E. Abe, B. S. Moonga, M. Zaidi, Calcineurin regulates bone formation by the osteoblast. *Proc. Natl. Acad. Sci. U.S.A.* **102**, 17130–17135 (2005).
55. L. E. Claes, C. A. Heigele, C. Neidlinger-Wilke, D. Kaspar, W. Seidl, K. J. Margevicius, P. Augat, Effects of mechanical factors on the fracture healing process. *Clin. Orthop. Relat. Res.* **355S**, S132–S147 (1998).
56. J. Barcik, M. Ernst, C. E. Dlaska, L. Drenchev, S. Zeiter, D. R. Epari, M. Windolf, Programable active fixator system for systematic in vivo investigation of bone healing processes. *Sensors* **21**, 17 (2020).
57. M. Windolf, V. Varjas, D. Gehweiler, R. Schwyn, D. Arens, C. Constant, S. Zeiter, R. G. Richards, M. Ernst, Continuous implant load monitoring to assess bone healing status—Evidence from animal testing. *Medicina* **58**, 858 (2022).
58. J. G. Wolynski, K. M. Labus, J. T. Easley, B. M. Notaroš, M. M. Ilić, C. M. Puttlitz, K. C. McGilvray, Diagnostic prediction of ovine fracture healing outcomes via a novel multi-location direct electromagnetic coupling antenna. *Ann. Transl. Med.* **9**, 1223–1223 (2021).
59. B. Kienast, B. Kowald, K. Seide, M. Aljudaibi, M. Faschingbauer, C. Juergens, J. Gille, An electronically instrumented internal fixator for the assessment of bone healing. *Bone Joint Res.* **5**, 191–197 (2016).
60. A. M. Rich, W. Rubin, S. Rickli, T. Akhmetshina, J. Cossu, L. Berger, M. Magno, K. M. Nuss, B. Schaller, J. F. Löffler, Development of an implantable sensor system for in vivo strain, temperature, and pH monitoring: Comparative evaluation of titanium and resorbable magnesium plates. *Bioact. Mater.* **43**, 603–618 (2025).
61. D. D. D'Lima, S. Patil, N. Steklov, J. E. Slamin, C. W. Colwell Jr., Tibial Forces Measured In Vivo After Total Knee Arthroplasty. *J. Arthroplasty* **21**, 255–262 (2006).
62. D. J. Wilson, R. L. Morgan, K. L. Hesselden, J. R. Dodd, S. W. Janna, M. J. Fagan, A single-channel telemetric intramedullary nail for in vivo measurement of fracture healing. *J. Orthop. Trauma* **23**, 702–709 (2009).
63. P. Jenkins, L. Nokes, The use of strain gauges to measurebone fracture healing—A review. *Curr. Orthop.* **8**, 116–118 (1994).
64. L. E. Claes, J. L. Cunningham, Monitoring the mechanical properties of healing bone. *Clin. Orthop. Relat. Res.* **467**, 1964–1971 (2009).
65. D. R. Carter, G. S. Beaupré, N. J. Giori, J. A. Helms, Mechanobiology of skeletal regeneration. *Clin. Orthop. Relat. Res.*, S41–S55 (1998).
66. P. Schwarzenberg, S. Darwiche, R. S. Yoon, H. L. Dailey, Imaging modalities to assess fracture healing. *Curr. Osteoporos. Rep.* **18**, 169–179 (2020).
67. R. Caldwell, M. G. Street, R. Sharma, P. Takmakov, B. Baker, L. Rieth, Characterization of Parylene-C degradation mechanisms: In vitro reactive accelerated aging model compared to multiyear in vivo implantation. *Biomaterials* **232**, 119731 (2020).
68. A. Lecomte, A. Degache, E. Descamps, L. Dahan, C. Bergaud, In vitro and in vivo biostability assessment of chronically-implanted Parylene C neural sensors. *Sens. Actuators B: Chem* **251**, 1001–1008 (2017).
69. Y. Zhang, A. D. Mickle, P. Gutruf, L. A. McIlvried, H. Guo, Y. Wu, J. P. Golden, Y. Xue, J. G. Grajales-Reyes, X. Wang, S. Krishnan, Y. Xie, D. Peng, C. J. Su, F. Zhang, J. T. Reeder, S. K. Vogt, Y. Huang, J. A. Rogers, R. W. Gereau IV, Battery-free, fully implantable optofluidic cuff system for wireless optogenetic and pharmacological neuromodulation of peripheral nerves. *Sci. Adv.* **5**, eaaw5296 (2019).
70. D. S. Margolis, G. Figueroa, E. B. Villalobos, J. L. Smith, C. J. Doane, D. A. Gonzales, J. A. Szivek, A large segmental mid-diaphyseal femoral defect sheep model: Surgical technique. *J. Invest. Surg.* **35**, 1287–1295 (2022).

Acknowledgments: We thank G. Book and J. Bohlman at the University of Arizona Nano Fabrication Center and S. Brueck at FEIG Electronics Inc. for the expertise. We also thank the staff at UA UAC for caring for large animal subjects (IACUC protocol numbers: 2021-0822 and 2023-1029). **Funding:** P.G. and D.M. acknowledge the support of DOD W81XWH-22-PRORP-ARA, NIH 1R01AR082394-01A1, and the Technology and Research Initiative Fund (TRIF). K.A.K. and G.F.R. acknowledge the support from the NIH Infection and Inflammation as Drivers of Aging (IIDA) training grant (1T32AG058503-04). **Author contributions:** Conceptualization and methodologies: K.A.K., G.F.R., D.S.M., and P.G. Software/firmware: K.A.K. Hardware design: K.A.K. and P.G. Investigation: K.A.K., G.F.R., D.L.P., D.A.G., A.M.M., and J.S. Visualization: K.A.K., G.F.R., D.L.P., A.M.M., J.S. Funding: D.S.M. and P.G. Administration and supervision: D.S.M. and P.G. Writing—original draft: K.A.K., G.F.R., D.A.G., D.S.M., and P.G. Writing—review and editing: K.A.K., G.F.R., D.S.M., and P.G. Data analysis: All authors contributed. **Competing interests:** The authors declare that they have no competing interests. **Data and materials availability:** All data needed to evaluate the conclusions in the paper are present in the paper and/or the Supplementary Materials. Other materials, e.g., custom written software, are available on our laboratory GitHub (github.com/Gutruf-Lab/) and/or ReData (DOI: 10.25422/azu.data.28735082), the University of Arizona's official public data archive (https://redata.arizona.edu/).

Submitted 9 October 2024
Accepted 7 April 2025
Published 9 May 2025
10.1126/sciadv.adt7488